Nano-chain amorphous CoB@porous $Ni(OH)_2$ ultrathin sheets as a high-performance supercapacitor material

Hui Wang, Jingjing Yan, Rongfang Wang, Shunxi Li, Dan J. L. Brett and Shan Ji

1 College of Chemistry and Chemical Engineering, Northwest Normal University, Lanzhou 730070, China

2 Electrochemical Innovation Lab, Dept. Chemical Engineering, University College London, London WC1E 7JE, UK

Abstract:

Ultrathin porous $Ni(OH)_2$ sheets were grown on the surface of nano-chain CoB as cores via a facile two-step solution-based method at ambient conditions. The resultant CoB@$Ni(OH)_2$ of 27.89 wt.% $Ni(OH)_2$ loading has a high specific capacitance of 1504.4 F g^{-1} at 0.5 A g^{-1}, 1293.7 F g^{-1} at 2 A g^{-1} and 746.8 F g^{-1} at 6 A g^{-1}. The excellent rate capability and stability of the material can be attributed to the CoB core's high electrical conductivity and stable cycling behavior, of which the latter may also contribute a significant capacitance contribution. The rational combination of these two materials in core-shell format is also an introduction to the study of CoB as a supercapacitor electrode material. Moreover, the facile and scalable method for the synthesis of CoB@$Ni(OH)_2$ places it as strong candidate for possible practical supercapacitor application.

Keywords: CoB; $Ni(OH)_2$; porous; core-shell; supercapacitor.

Introduction

High-performance supercapacitors are widely applied in the fields of mobile electronics, backup power supplies, and electric vehicles due to their high power density, fast charge/discharge, and long cycle life.[1] Transition metal oxides and hydroxides, such as RuO_2, MnO_2, Co_3O_4, NiO and $Ni(OH)_2$, are examples of pseudocapacitive materials characterized by high reversible redox-based capacitance via oxidation state transitions.[2] However, due to their low electrical conductivity, their observed specific capacitance is much lower than that might be expected from their high theoretical specific capacities, especially at high current densities required for supercapacitor performance. As a result, high specific capacitance in pseudocapacitive oxide material is usually limited to very thin films.[3] Such films are impractical for commercial cells due to the much larger relative mass and volume contribution of the current collectors the films are formed on.

Physically attaching pseudocapacitive oxide materials to materials such as particulate carbon[4] and conducting polymers,[5] either at the nano or micrometer scale of particle size, is frequently employed to improve oxide conductivity. Some reports have also shown that the practical capacitance of oxides is significantly improved using metal and metal alloys as conductive supports.[6, 7, 8, 9] Chen and co-workers showed that RuO_2 and MnO_2 supported on nanoporous Au or NiMn alloy, could reach high specific capacitances close to their theoretical values due to the provision of fast ionic conduction and excellent electron-proton transport.[8] However, both the high material cost of nanoporous Au and elaborate fabrication process of

electrochemical polarization narrows the practical applicability of these oxide@porous metal/alloy electrodes.[9] An oxy/hydroxide@ low-cost metal/alloy combination achieving the same high specific capacitance and cyclic stability, particularly through a facile large-scale production method, is therefore of obvious interest.

Various reports show that transition metal borides, particularly CoB alloys, exhibit high specific capacitance and cycling stability as anode materials for aqueous batteries in alkaline electrolyte.[10-12] In contrast, their performance as supercapacitor material has received surprisingly little attention,[13] with CoB being no exception. However, CoB alloys have high electronic conductivity in the order of 10^3 S cm^{-1} (similar to Co metal), which is around ten orders of magnitude higher than that of oxides/hydroxides (e.g. $Ni(OH)_2$ in the order of 10^{-15} S cm^{-1}).[11] This suggests CoB should either have high rate capability as a capacitance material and/or be useful as a conductive support for other capacitance material. In particular, $Ni(OH)_2$, while low in conductivity, has high theoretical specific capacity (289.1 mAh/g), as well as well-defined redox behavior in alkaline electrolyte, and can form layered structures with large interlayer spacing theoretically supportive of high capacitance.[14] In the present study, we scrupulously aimed for a particle architecture that combines $Ni(OH)_2$ nanoflakes supported on CoB nanochains. Through this novel structural design, the material has both high rate capability and high specific capacitance.

Figure S1 shows the powder X-ray diffraction (XRD) patterns of CoB and CoB@$Ni(OH)_2$. The XRD pattern of CoB has wide peak dispersion indicative of

amorphous structure. In the case of CoB@$Ni(OH)_2$, beside the dispersion peak, two new small peaks appear at 2θ ~ 34.0 and 60.5^o corresponding to the (100) and (111) planes of hexagonal phase ß–$Ni(OH)_2$ (JCPDS Card No. 1–1047), thus indicating hybrid particle structure was obtained. Bulk composition analyses of the two samples by inductively coupled plasma (ICP), found the Co:B atomic ratio in the CoB sample to be ca. 2.2:1, and the Co:B:Ni atomic ratio in the CoB@$Ni(OH)_2$ sample to be ca. 10.43:4.74:1. The estimated mass percentage of $Ni(OH)_2$ in the CoB@$Ni(OH)_2$ sample is ca. 12.26%.

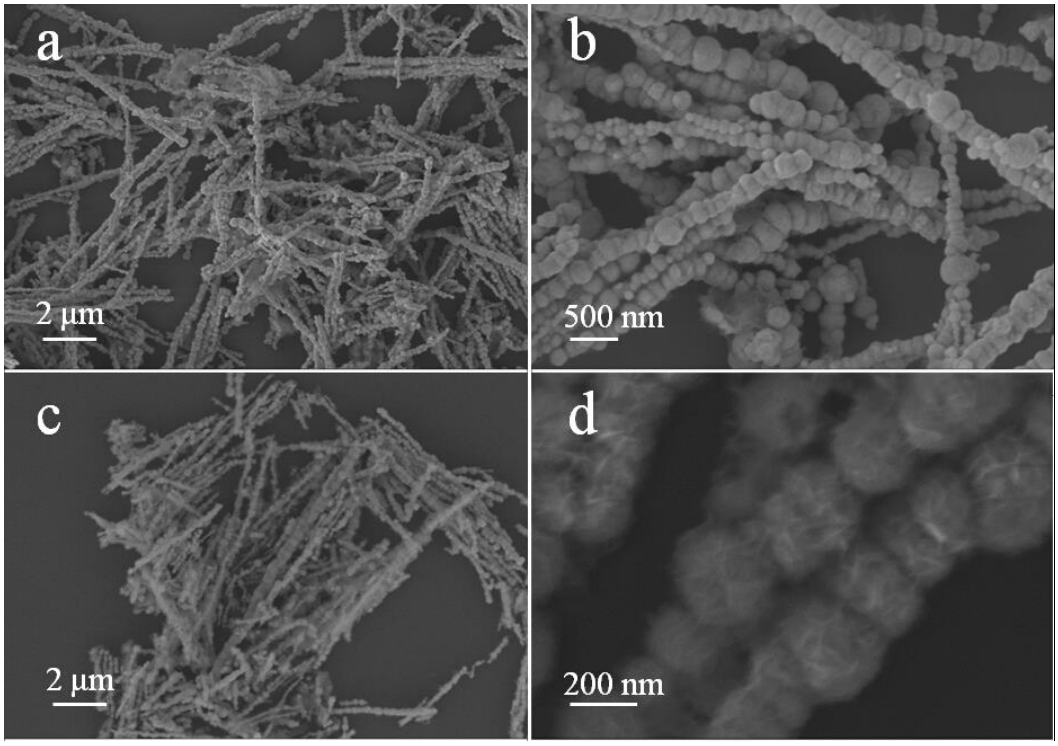

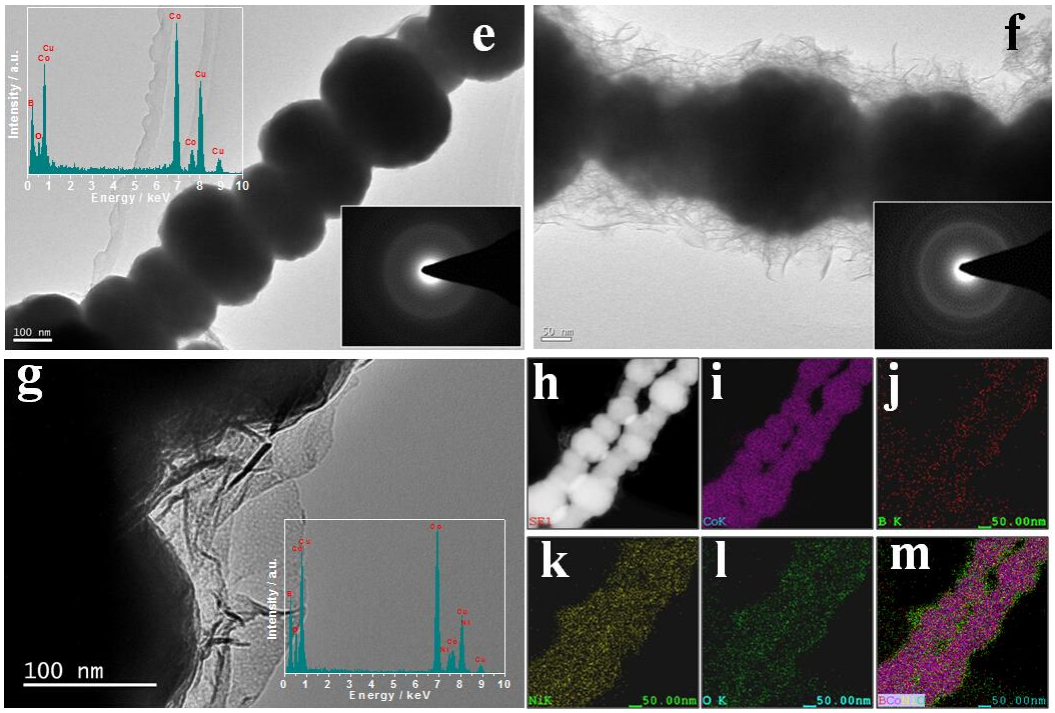

Figure 1. SEM images of (a,b) CoB and (c,d) CoB@Ni(OH)$_2$; TEM images of (e) CoB and (f, g) CoB@Ni(OH)$_2$; SAED images lower right insets (e and f); EDS plots upper left inset (e) and lower right (g); (h) STEM elemental mapping image of CoB@Ni(OH)$_2$, (i) Co, (j) B, (k) Ni, (l) O; and (m) overlapped elemental mapping image of Co, B, Ni and O in CoB@Ni(OH)$_2$.

Figure 1a-d shows scanning electron microscopy (SEM) images of CoB and CoB@Ni(OH)$_2$. CoB formed uniform bead-like particles of ~50 to 250 nm that joined together as long chains (Figure 1a). This underlying chain structure was clearly maintained after Ni(OH)$_2$ deposition, which formed a continuous covering on the CoB surface as nanoflakes (Figure 1c,b). The nanoflake structure is clearly visible in the transmission electron microscopy (TEM) images (Figure 1f and g). Energy dispersive spectroscopy (EDS) of CoB (upper left corner inset in Figure 1e) revealed the

presence of Co and B elements, and its selected area electron diffraction (SAED) pattern (lower right corner inset) formed a continuous hollow ring diffraction pattern typical of amorphous material[15], which correlates with the XRD result. The enlarged TEM image of CoB@$Ni(OH)_2$ (Figure 1g) shows the $Ni(OH)_2$ flocculent layer comprised ultrathin sheets, and the SAED pattern (lower right corner inset in Figure 1f) displays several rings indicating $Ni(OH)_2$ had polycrystalline structure. The EDS pattern of CoB@$Ni(OH)_2$ (lower right corner inset in Figure 1g) revealed the presence of Co, B, Ni and O elements, and the scanning TEM (STEM) image (Figure 1h) and electron energy loss spectroscopic mapping (Figure 1i-l) shows uniform distribution of Co, B, Ni and O elements, which with overlapping (Figure 2m) reveals the core-shell structure distribution of these elements.

X-ray photoelectron spectroscopy (XPS) analysis was carried out to identify the elemental composition and chemical states of the elements on the surface of CoB@$Ni(OH)_2$. The survey spectra of CoB and CoB@$Ni(OH)_2$ (**Figure S2**a) revealed the presence of Co and B elements in CoB and Co, B, Ni, O in CoB@$Ni(OH)_2$. Figure S2b shows the Co 2p XPS spectrum of CoB contains the two characteristic peaks of Co $2p_{3/2}$ (781.8 eV) and Co $2p_{1/2}$ (797.8 eV) along with shake-up satellites. The two peaks clearly shift to higher binding energy compared to that of metallic Co or Co hydro/oxides,[16] resulting possibly from electron transfer from Co to B atoms. In contrast, shake-up satellites in the Co 2p XPS spectrum of CoB@$Ni(OH)_2$ can hardly be observed, most likely due to signal suppression by the $Ni(OH)_2$ shell, which offers further evidence of the CoB@$Ni(OH)_2$ core-shell

structure. Similarly, the B 1s XPS signal (Figure S2c) clearly appears in the CoB plot, but is absent in the CoB@$Ni(OH)_2$ plot. The B 1s XPS spectrum of CoB displayed two peaks, one at low binding energy (188.0 eV) that may correlate to the free form of elemental B, and the other at high binding energy (192.0 eV) to boron oxide.[17] The Ni XPS signal (Figure S2d) for CoB@$Ni(OH)_2$ has two intense peaks centered at 855.8 eV and 873.7 eV corresponding to Ni $2p_{3/2}$ and Ni $2p_{1/2}$ respectively, followed by clear satellite signals at high binding energy. These bands are characteristic of the $Ni(OH)_2$ phase and are consistent with previous reports.[18, 19] In the O 1s spectrum of the $Ni(OH)_2$ (Figure S2e), the main peak of 529.4 eV corresponds to metal-O bonds.[20]

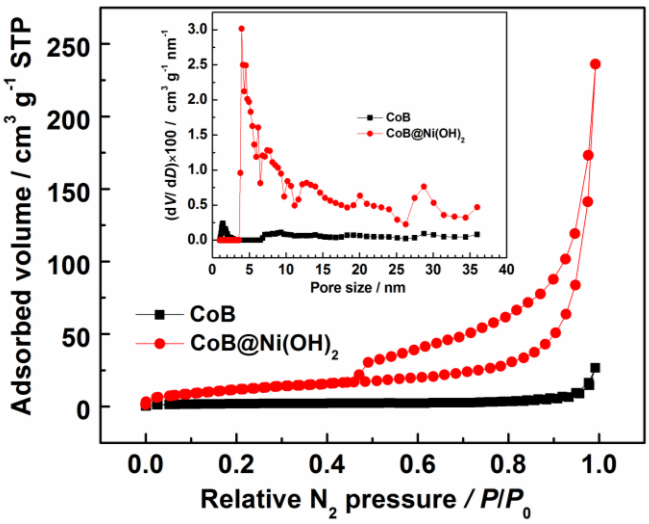

Figure 2. N_2 isotherms and (Inset) the pore size distribution of CoB and CoB@$Ni(OH)_2$.

N_2 isotherm analysis (**Figure 2**) was used to evaluate the porosity of CoB and CoB@$Ni(OH)_2$. With increase of relative pressure, the adsorbed N_2 volume by CoB

was much less than that of CoB@$Ni(OH)_2$, indicating that CoB@$Ni(OH)_2$ has higher porosity than CoB. The N_2 isotherm of CoB forms the typical I isotherm shape of IUPAC classification, and the absence of uptakes and hysteresis loop suggests limited presence of pores.[21] In contrast, CoB@$Ni(OH)_2$ produced a type II isotherm with an hysteresis loop starting at 0.47 relative pressure, indicating the presence of mesopores. The overall pore size distribution for CoB@$Ni(OH)_2$, was thus in the mesopore size range with few micropores present (inset Figure 2). Furthermore, the BET surface area of CoB and CoB@$Ni(OH)_2$ was 6.6 and 42.5 $m^2\ g^{-1}$ respectively, showing considerable surface area increase after $Ni(OH)_2$ deposition due to the porous structure of the $Ni(OH)_2$ shell.

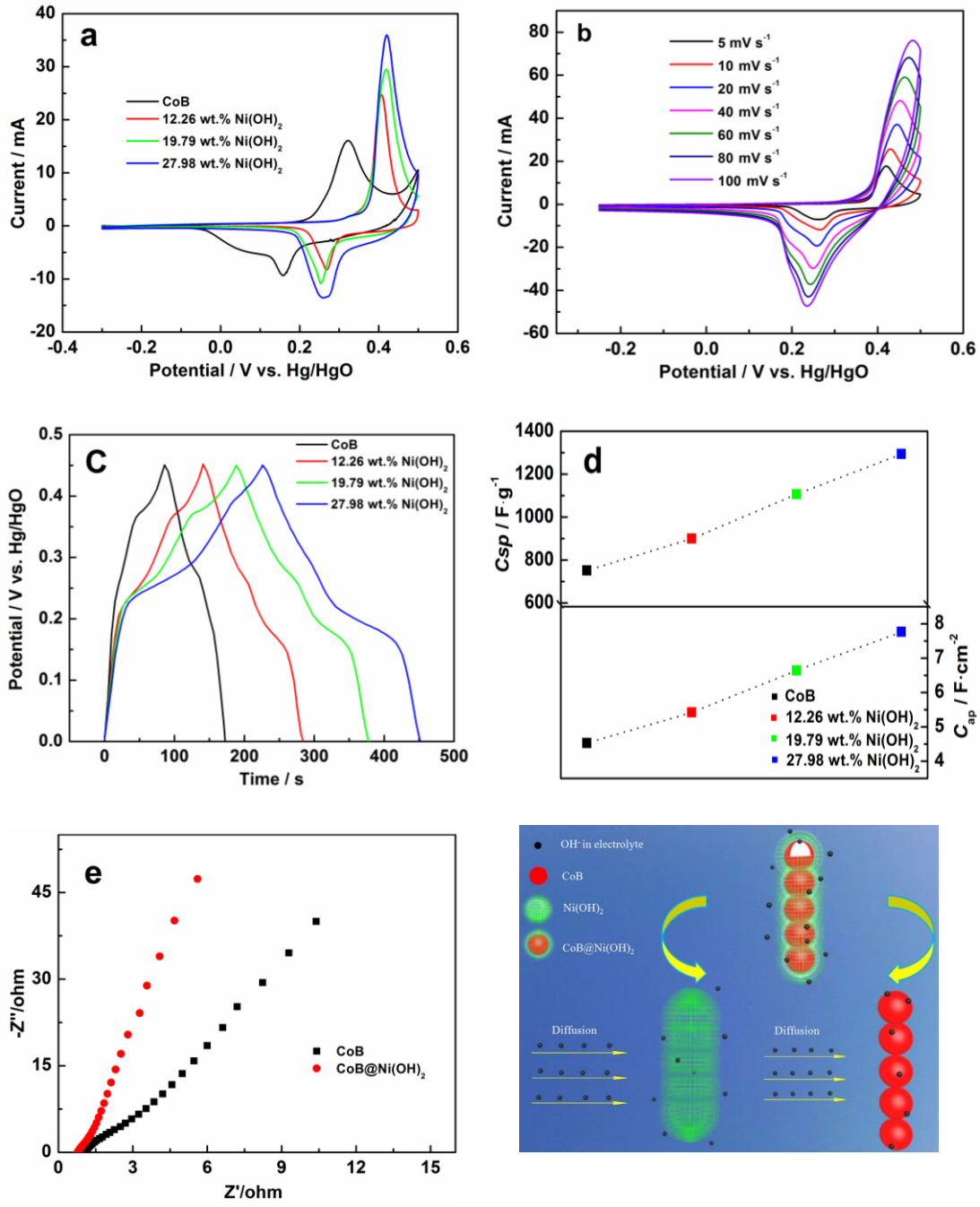

Figure 3. (a) CV plots of the CoB and CoB@$Ni(OH)_2$ electrodes at scan rate of 50 mV s^{-1}; (b) CV plots of the CoB@$Ni(OH)_2$ electrode with 27.98 wt.% $Ni(OH)_2$ at different scan rates from 5 to 100 mV s^{-1}; (c) galvanostatic charge-discharge curves of the CoB and CoB@$Ni(OH)_2$ electrodes with different $Ni(OH)_2$ content at current density of 2 A g^{-1}; (d) variation in specific capacitance of the CoB@$Ni(OH)_2$ hybrid

with the mass percentage of the $Ni(OH)_2$ shell; (e) Comparison of Nyquist plots of the CoB and 27.98 wt.% CoB@$Ni(OH)_2$ electrodes; (f) Schematic of the CoB@$Ni(OH)_2$ hybrid, showing CoB core and $Ni(OH)_2$.

To evaluate the capacitive influence of $Ni(OH)_2$ mass loading on CoB, $NiCl_2$ concentration was varied during synthesis to form different CoB@$Ni(OH)_2$ hybrids of varying $Ni(OH)_2$ wt.%. Their bulk composition, physical characterization including XRD, SEM, N_2 and isotherms are provided in **Table S1** and **Figure S3-5**. As seen in Table S1, the maximum mass percentage of $Ni(OH)_2$ that can be achieved was 27.89 wt.% at an $NiCl_2$ concentration of 0.2 mmol, while retaining morphology and porous structure (Figure S3-5).

The electrochemical behavior of CoB and CoB@$Ni(OH)_2$ was studied using cyclic voltammetry (CV) and galvanostatic cycling, both using three-electrode cell configurations in 6 mol L^{-1} KOH solution. **Figure 4**a shows the CV plots of the CoB and CoB@$Ni(OH)_2$ electrodes after activation at a scan rate of 5 mV s^{-1}. It should be noted that $Co(OH)_2$ forms on the CoB surface during the activation process in alkaline solution.[12, 22] The CV plot of CoB produced an oxidation peak at 0.347 V and a corresponding reduction peak at 0.151 V,[23, 24] whereas CoB@$Ni(OH)_2$ produced an oxidation peak at ca. 0.430 V and a reduction peak at 0.265 V. The corresponding reversible reactions associated with these peaks respectively were considered to be:

$$Co(OH)_2 + OH^- \rightarrow CoOOH + H_2O + e^- \quad (1)$$

$$Ni(OH)_2 + OH^- \rightarrow NiOOH + H_2O + e^- \quad (2)$$

Notably, all the CV curves of CoB@$Ni(OH)_2$ show larger voltammetric current

than that of CoB, suggesting strong capacitive contribution from the $Ni(OH)_2$ shell. Voltammetric current increase occurred with increase of $Ni(OH)_2$ mass content, indicating CoB@$Ni(OH)_2$ containing the highest $Ni(OH)_2$ content of 27.98 wt.% would also have the highest capacitance. Moreover, the high current response from the 27.98 wt.% electrode (Figure 3b) maintained the same CV peak shape and potential gap between oxidation and reduction peaks as scan rate increased, indicating CoB@$Ni(OH)_2$ had good capacitive reversibility.[24, 25]

Figure 3c shows the galvanostatic charge-discharge plots of CoB and CoB@$Ni(OH)_2$ at a current density of 2 A g^{-1}. In all cases, the nonlinear charge curves are asymmetric to their corresponding discharge curves, which is commonly observed for pseudocapacitive materials.[26] Compared to the pristine CoB nanochains, all CoB@$Ni(OH)_2$ hybrids produced high capacitance discharge curves, which correlates to the high current responses of their CV curves. Specific capacitance (C_{sp}) was calculated from the discharge curves considering total CoB and $Ni(OH)_2$ mass content Figure 4d. All the CoB@$Ni(OH)_2$ hybrids produced higher C_{sp} than that of CoB, which demonstrates the high capacitance contribution of the $Ni(OH)_2$ shell. Specific capacitance increased with increased $Ni(OH)_2$ loading from 12.26 wt.% to 27.89 wt.% (at 1293.7 F g^{-1}); equating to 7.76 F cm^{-2} with respect to relative electrode surface area (C_{ap}, Figure 3d). The specific capacitance for CoB at 2 A g^{-1} was 750 F g^{-1}, and thus considerably smaller than that of the CoB@$Ni(OH)_2$ containing the highest mass percentage of $Ni(OH)_2$. Figure 3e compares the electrochemical impedance spectra (EIS) of the two materials. Here, it can be seen the

CoB@$Ni(OH)_2$ hybrid clearly has decreased overall equivalent series resistance (Rs, the real axis intercept) than CoB due to its higher specific capacitance.[27]

The specific capacitance of $Ni(OH)_2$@Mn_2O_3 hybrid with 27.89 wt.% $Ni(OH)_2$ is quite attractive when compared with previously reported values of other core/$Ni(OH)_2$-shell-based electrodes [18, 28] (**Table S2**). In particular, although some binder-free electrodes based on other core/$Ni(OH)_2$-shell hybrid materials such as TiN@ $Ni(OH)_2$,[7] ZnO@$Ni(OH)_2$,[29] $NiCo_2S_4$@$Ni(OH)_2$,[30] $NiMoO_4$@$Ni(OH)_2$,[31] $ZnCo_2O_4$@$Ni(OH)_2$ [32] have high specific capacitance, in general, complex synthesis steps and the limited loading density of the electrodes have predictably high manufacturing cost, thus hindering large-scale application possibilities. Therefore among the particle-based electrodes materials thus far produced, the present study's material of 1293.7 F g^{-1} at 2 A g^{-1} is a significant achievement within the cost affective category considering its simple synthesis and high specific capacitance at high current density.

Three physically properties of the $Ni(OH)_2$/metal alloy combination, owing to its unique morphology and composition, may account for its overall high specific capacitance. Firstly, the $Ni(OH)_2$ nanoflakes grown *in situ* on the CoB nanochains are well separated. This provides unhindered access for surface absorption and movement of OH^- electrolyte ions involved in capacitance. Secondly, as illustrated in Figure 3f, the electrolyte can theoretically reach the surface of the CoB core through the many mesopores in the $Ni(OH)_2$ shell, as indicated by its pore size distribution (Figure 2 inset). Here, since $Co(OH)_2$ forms on the CoB surface during activation in alkaline

solution,[12, 22] mesopores in $Ni(OH)_2$ could allow OH^- electrolyte ions access to $Co(OH)_2$ to participate in capacitance through Reaction (1), which suggests that the specific capacitance of CoB@$Ni(OH)_2$ may derive from both CoB and $Ni(OH)_2$. Thirdly, CoB provides a highly conductive support in CoB@$Ni(OH)_2$ for rapid electron transport, which facilitates high specific capacitance at high current density [8].

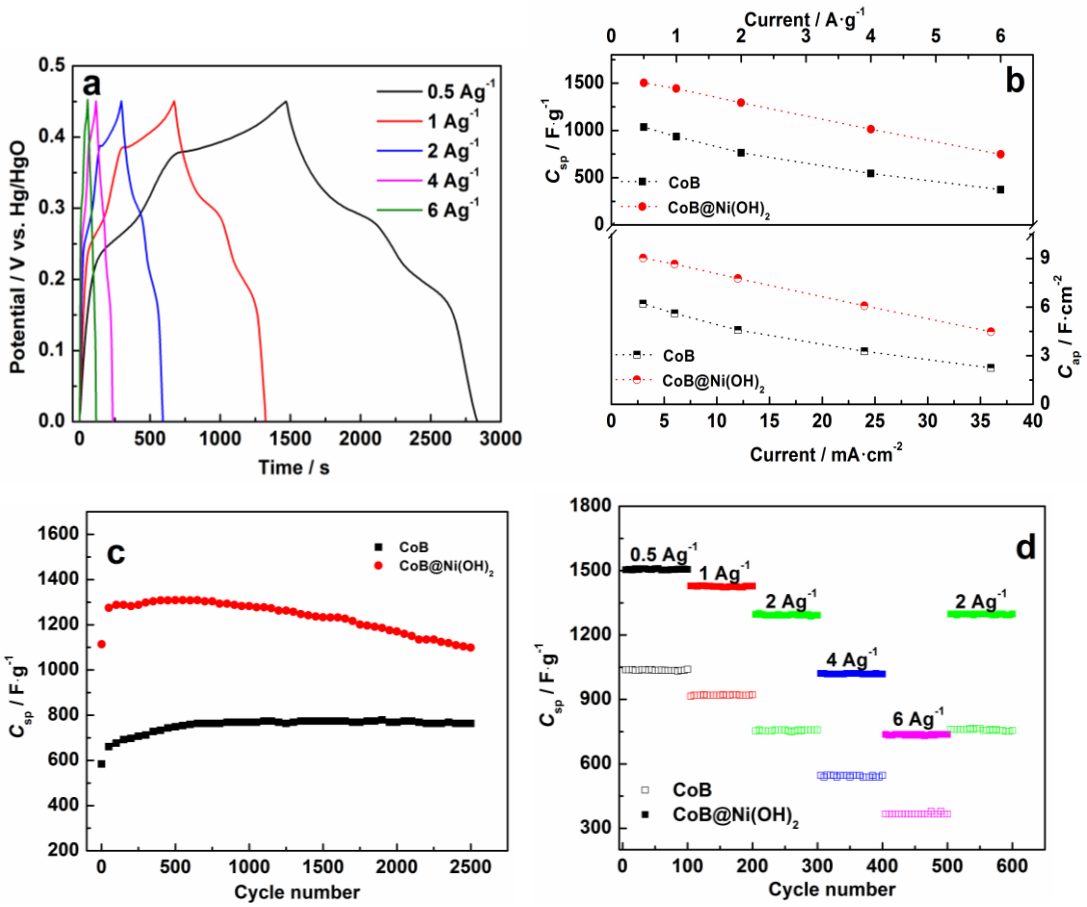

Figure 4. (a) Galvanostatic charge-discharge curves of CoB@$Ni(OH)_2$ (27.89 wt.%) at different current densities (0.5, 1, 2, 4, and 6 A g^{-1}); (b) Current density dependence of specific capacitance of CoB and CoB@$Ni(OH)_2$ (27.89 wt.%); (c) Cycling performance of both CoB and CoB@$Ni(OH)_2$ electrodes during 2500 cycles at 2 A g^{-1};

and (d) Cycling stability of both CoB and CoB@$Ni(OH)_2$ at different current densites.

Figure 4 and **Figure S7** compare the rate capabilities of CoB and CoB@$Ni(OH)_2$ (27.89 wt.%) at increasing current densities. Drop in specific capacitance occurred on both materials with current density increase, correlating with literature on other core/$Ni(OH)_2$-shell-based materials.[18, 28, 29-32] Within the current range of 0.5 A g^{-1} to 6 A g^{-1} (i.e. 3 mA cm^{-2} to 36 mA cm^{-2}), CoB@$Ni(OH)_2$ maintained a consistently higher specific capacitance than the CoB (Figure 4b). At 6 A g^{-1}, the specific capacitance of CoB@$Ni(OH)_2$ (746.8 F g^{-1}) was 49.7% of that measured at 0.5 A g^{-1}. Therefore, at 6 A g^{-1} the specific capacity of CoB@$Ni(OH)_2$ was still ~2.0 fold higher than that of CoB (373.5 F g^{-1}) at 0.5 A g^{-1}. The overall ~50% drop in specific capacitance for both materials over the 12-fold increase from 0.5 to 6 A g-1 reveals both materials have high conductivity.

The cycle life of CoB and CoB@$Ni(OH)_2$ (27.89 wt.%) was evaluated over 2500 continuous charge-discharge cycles at a current density of 2 A g^{-1} (Figure 4c). Interestingly, the specific capacitance of both electrodes gradually increased during the first 200 cycles, which is likely due in part to the activation processes involved the formation of $Co(OH)_2$.[12, 33] Both CoB and CoB@$Ni(OH)_2$ hybrid exhibit good long-term electrochemical stability, as further evident from their very stable charge–discharge curves for the comparison between the first and last 8 cycles (**Figure S8**, with ~99% of coulombic efficiency). The specific capacitance loss for CoB@$Ni(OH)_2$ after 2500 cycles was 15%. By contrast, 100% specific capacitance was retained for CoB, and this remarkable cycling stability appears to derive from the

stability of the capacitive $Co(OH)_2$ passivation layer, which interestingly also appears to prevent B dissolving (reaction (3)), which would no doubt result in capacitance loss:

$$B + 4OH^- \rightarrow H_2BO^{3-} + H_2O + 3\,e^- \quad (3)$$

The stability of CoB@$Ni(OH)_2$ hybrid is also much greater than that of other reported core/$Ni(OH)_2$-shell hybrid materials such as TiN@ $Ni(OH)_2$,[7] $NiCo_2S_4$@$Ni(OH)_2$,[30] $NiMoO_4$@$Ni(OH)_2$,[31] $ZnCo_2O_4$@$Ni(OH)_2$,[32] and $NiCo_2O_4$@$Ni(OH)_2$ [34] as listed in Table S1. Therefore, CoB as the core in the core-shell CoB@$Ni(OH)_2$ hybrid clearly promotes stability during cycling. To further explore the durability of CoB@$Ni(OH)_2$ and CoB, cycling was carried out at progressively increased current densities (Figure 4d) and then returned to 2 A g^{-1}. Remarkably, after 500 cycles at different current densities, and despite the abrupt changes in current density, the capacitance of CoB@$Ni(OH)_2$ hybrid returned to 1276.5 F g^{-1} at 2 A g^{-1} , equating to ~99 % of the initial capacitance (1293.7, F g^{-1}). Furthermore, this capacitance maintained its level for another 100 cycles without noticeable decrease. Therefore, this final result indicates CoB@$Ni(OH)_2$ has excellent durability at different current densities, which is an important merit for practical energy storage devices.

Conclusions

A facile, *in situ* synthesis method at room temperature was achieved to directly grow porous $Ni(OH)_2$ nano-sheets on the surface of nano-chain CoB alloy for use as capacitive supercapacitor material. In this particular architecture, both the $Ni(OH)_2$

shell and CoB core may act in capacitive charge storage, while the CoB core also serves as a conductive backbone for electron transport. Electrochemical evaluation revealed that the optimized CoB@$Ni(OH)_2$ electrode delivers a high specific capacitance (1504.4 F g^{-1}) at 0.5 A g^{-1} with good rate capability and cyclic stability. The excellent performance is attributed to synergetic contribution from the CoB core and the porous $Ni(OH)_2$ shell. In conclusion, the uncomplicated synthesis method could be readily scalable, thus offering a means to produce material of high specific capacitance and high stability by a practical and cost effective means.

Acknowledgements

The authors would like to thank the National Natural Science Foundation of China (21363022 and 51362027) for financially supporting this work.

References

[1] Y. Q. Zhang, L. Li, S. J. Shi, Q. Q. Xiong, X. Y. Zhao, X. L. Wang, C. D. Gu, J. P. Tu, J. Power Sources 2014, 256, 200; Y. Du, X. Zhao, Z. Huang, Y. Li, Q. Zhang, RSC Advance 2014, 4, 39087.

[2] J. Liu, J. Jiang, C. Cheng, H. Li, J. Zhang, H. Gong, H. J. Fan, Adv. Mater. 2011, 23, 2076; H. Jiang, C. Li, T. Sun, J. Ma, Chem. Commun. 2012, 48, 2606.

[3] C. Zhao, W. Zheng, Frontiers in Energy Research 2015, 3.

[4] Y. Zou, I. A. Kinloch, R. A. Dryfe, ACS Appl. Mater. Interfaces 2015, 7, 22831; Y. Zhao, Y. Meng, P. Jiang, J. Power Sources 2014, 259, 219; R. Kumar, R. K. Singh, P. K. Dubey, D. P. Singh, R. M. Yadav, ACS Appl. Mater. Interfaces 2015, 7, 15042.

[5] X. Zhang, X. Zeng, M. Yang, Y. Qi, ACS Appl. Mater. Interfaces 2014, 6, 1125; X. Zhang, L. Ji, S. Zhang, W. Yang, J. Power Sources 2007, 173, 1017; J.-G. Wang, Y. Yang, Z.-H. Huang, F. Kang, J. Power Sources 2012, 204, 236.

[6] Q. Lu, M. W. Lattanzi, Y. Chen, X. Kou, W. Li, X. Fan, K. M. Unruh, J. G. Chen, J. Q. Xiao, Angewandte Chemie 2011, 123, 6979; W. Ni, B. Wang, J. Cheng, X. Li, Q. Guan, G. Gu, L. Huang, Nanoscale 2014, 6, 2618.

[7] H. Yi, X. Chen, H. Wang, X. Wang, Electrochim. Acta 2014, 116, 372.

[8] X. Lang, A. Hirata, T. Fujita, M. Chen, Nat. Nanotechnol. 2011, 6, 232; L. Y. Chen, Y. Hou, J. L. Kang, A. Hirata, T. Fujita, M. W. Chen, Advanced Energy Materials 2013, 3, 851.

[9] J. Kang, A. Hirata, H. J. Qiu, L. Chen, X. Ge, T. Fujita, M. Chen, Adv. Mater. 2014, 26, 269.

[10] Y. D. Wang, X. P. Ai, Y. L. Cao, H. X. Yang, Electrochem. Commun. 2004, 6, 780.
[11] H. X. Yang, Y. D. Wang, X. P. Ai, C. S. Cha, Electrochem. Solid-State Lett. 2004, 7, A212.
[12] Y. D. Wang, X. P. Ai, H. X. Yang, Chem. Mater. 2004, 16, 5194.
[13] W. Zhang, Y. Tan, Y. Gao, J. Wu, B. Tang, J. Zhao, RSC Advances 2014, 4, 27800.
[14] Z. Wang, X. Wang, Y. X. Zhao, C. M. Zhao, W. T. Zheng, Journal of Nano Research 2012, 20, 53; S.-i. Yamazaki, T. Ioroi, K. Tanimoto, K. Yasuda, K. Asazawa, S. Yamaguchi, H. Tanaka, J. Power Sources 2012, 204, 79.
[15] Y. Ma, R. Wang, H. Wang, V. Linkov, S. Ji, PCCP 2014, 16, 3593.
[16] X. T. Zhang, H. Wang, J. L. Key, V. Linkov, S. Ji, X. L. Wang, Z. Q. Lei, R. F. Wang, J. Electrochem. Soc. 2012, 159, B270; W. Huang, Z. Zuo, P. Han, Z. Li, T. Zhao, J. Electron. Spectrosc. Relat. Phenom. 2009, 173, 88.
[17] B. Crist, Mountain View, CA 1999.
[18] Qingqing Ke, C. Guan, M. Zheng, Y. Hu, K.-h. Ho, J. Wang, Journal of Materials Chemistry A 2015, 3, 9538.
[19] J.-H. Zhong, A.-L. Wang, G.-R. Li, J.-W. Wang, Y.-N. Ou, Y.-X. Tong, J. Mater. Chem. 2012, 22, 5656.
[20] Y. Ma, R. Wang, H. Wang, J. Key, S. Ji, J. Power Sources 2015, 280, 526; P. Tao, M. Shao, C. Song, S. Wu, M. Cheng, Z. Cui, J. Ind. Eng. Chem. 2014, 20, 3128.
[21] Y. Ma, H. Wang, W. Lv, S. Ji, B. G. Pollet, S. Li, R. Wang, RSC Advances 2015, 5, 68655.
[22] Y. Liu, Y. Wang, L. Xiao, D. Song, Y. Wang, L. Jiao, H. Yuan, Electrochim. Acta 2008, 53, 2265.
[23] L. Ma, H. Zhou, X. Shen, Q. Chen, G. Zhu, Z. Ji, RSC Advances 2014, 4, 53180.
[24] C. Yuan, X. Zhang, L. Hou, L. Shen, D. Li, F. Zhang, C. Fan, J. Li, J. Mater. Chem. 2010, 20, 10809.
[25] R. Wang, Y. Ma, H. Wang, J. Key, D. Brett, S. Ji, S. Yin, P. K. Shen, Journal of Materials Chemistry A 2016, 4, 5390.
[26] K. Wang, C. Zhao, S. Min, X. Qian, Electrochim. Acta 2015, 165, 314; W. Sun, X. Rui, M. Ulaganathan, S. Madhavi, Q. Yan, J. Power Sources 2015, 295, 323.
[27] H. Chen, S. Zhou, L. Wu, ACS Appl. Mater. Interfaces 2014, 6, 8621; H. Chen, L. Hu, Y. Yan, R. Che, M. Chen, L. Wu, Advanced Energy Materials 2013, 3, 1636.
[28] C. H. Tang, X. Yin, H. Gong, ACS Appl. Mater. Interfaces 2013, 5, 10574; W. Tian, X. Wang, C. Zhi, T. Zhai, D. Liu, C. Zhang, D. Golberg, Y. Bando, Nano Energy 2013, 2, 754; W. Zhou, X. Cao, Z. Zeng, W. Shi, Y. Zhu, Q. Yan, H. Liu, J. Wang, H. Zhang, Energy Environ. Sci. 2013, 6, 2216.
[29] I. Shakir, Z. Ali, J. Bae, J. Park, D. J. Kang, RSC Advances 2014, 4, 6324.
[30] J. Zhang, H. Gao, M. Y. Zhang, Q. Yang, H. X. Chuo, Appl. Surf. Sci. 2015, 349, 870.
[31] Ge Jiang, Mingyi Zhang, Xueqing Li, Hong Gao, RSC Advances 2015, 5, 69365.
[32] H. X. Chuo, H. Gao, Q. Yang, N. Zhang, W. B. Bu, X. T. Zhang, Journal of Materials Chemistry A 2014, 2, 20462.
[33] Y. Liu, Y. Wang, L. Xiao, D. Song, L. Jiao, H. Yuan, Electrochem. Commun. 2007, 9, 925.
[34] W. Li, L. Xin, X. Xu, Q. Liu, M. Zhang, S. Ding, M. Zhao, X. Lou, Sci Rep 2015, 5, 9277.